Asparagine drives immune evasion in bladder cancer via RIG-I stability and type I IFN signaling

Wenjie Wei[1,2,3], Hongzhao Li[1], Shuo Tian[1,2,3], Chi Zhang[1,2,3], Junxiao Liu[1,2,3], Wen Tao[1,2,3], Tianwei Cai[1,2,3], Yuhao Dong[1,2,3], Chuang Wang[1,2,3], Dingyi Lu[4], Yakun Ai[5], Wanlin Zhang[5], Hanfeng Wang[1,2,3], Kan Liu[1], Yang Fan[1], Yu Gao[1], Qingbo Huang[1], Xin Ma[1], Baojun Wang[1], Xu Zhang[1], Yan Huang[1,2]

[1]Department of Urology, The Third Medical Center, Chinese PLA General Hospital, Beijing, China.
[2]Department of Urology Laboratory, Chinese PLA General Hospital, Beijing, China.
[3]Medical School of PLA, Beijing, China.
[4]State Key Laboratory of Proteomics, Institute of Basic Medical Sciences, National Center of Biomedical Analysis, Beijing, China.
[5]Department of Pathology, The Third Medical Center, Chinese PLA General Hospital, Beijing, China.

Authorship note: Wenjie Wei and Hongzhao Li contributed equally as co-authors of this article.

Correspondence:
Yan Huang, Department of Urology, The Third Medical Centre, Chinese PLA General Hospital, Beijing, 100039, China. Phone: 86-10-66938008; E-mail: dr.huangyan301@foxmail.com; Xu Zhang, E-mail: xzhang301@163.com; and Baojun Wang, E-mail: baojun40009@126.com;

Running title: ASNS servers as a valuable biomarker for ICIs response.

Conflicts of Interest: The authors have declared that no conflict of interest exists.

Abstract

Tumor cells often employ many ways to restrain type I interferon signaling to evade immune surveillance. However, whether cellular amino acid metabolism regulate this process remains unclear and its effects on antitumor immunity are relatively unexplored. Here, we find that asparagine inhibits IFN-I signaling and promotes immune escape in bladder cancer. Depletion of asparagine synthetase (ASNS) strongly limits in vivo tumor growth in a CD8+ T cell-dependent manner and boosts immunotherapy efficacy. Moreover, clinically approved ASNase synergizes with anti-PD-1 therapy in suppressing tumor growth. Mechanistically, asparagine can directly bind to RIG-I and facilitate CBL-mediated RIG-I degradation, thereby suppressing IFN signaling and antitumor immune responses. Clinically, tumors with higher ASNS expression show decreased responsiveness to ICIs therapy. Together, our findings uncover asparagine as a natural metabolite to modulate RIG-I-mediated IFN-I signaling, providing the basis for developing the combinatorial use of ASNase and anti-PD-1 for bladder cancer.

Introduction

Bladder cancer is one of the most prevalent tumors in the urinary system and is responsible for nearly 165,000 deaths every year worldwide (1). Approximately 25% of patients present with muscle invasive disease and the relative 5-year overall survival rate of advanced-stage bladder cancer is low, with limited therapeutic advances (2, 3). Radical cystectomy and cisplatin-based chemotherapy are recommended for the standard treatment option for muscle-invasive bladder cancer (MIBC) (4). In recent years, immune checkpoint inhibitors (ICIs) have achieved tremendous clinical breakthroughs in cancer immunotherapy (5, 6). Though ICIs have shown durable responses in a subset of patients with bladder cancer, the overall response rate is only ~15–25% (7, 8), which increases the demand for biomarkers of response and effective targeted therapies to enhance ICIs therapy.

Emerging evidence indicates that the tumor microenvironment (TME) is a complex system that determines the occurrence of tumor immune responses (9, 10). CD8+ T cells play a central role in cancer immunotherapy and elicit antitumor activity by directly recognizing and killing tumor cells (11, 12). Patients with high CD8+ T cells infiltration in TME are associated with a survival benefit in several tumor types and better response to immunotherapy (13). Previous studies have reported that type I Interferon (IFN-I) are essential for activating adaptive immune response and play a crucial role in CD8+ T cells infiltration and immunogenic tumor rejection (14, 15). Given that RIG-I-like receptors (RLRs) are critical for activating the IFNs pathway and triggering immunogenic cell death, stimulation of retinoic acid-inducible gene-I (RIG-I) or melanoma differentiation-associated gene 5 (MDA5) signaling has emerged as a strategy for antitumor immunity (16, 17). However, tumor cells often employ multiple strategies to evade immunosurveillance by inhibiting RLRs-mediated signaling pathway (18, 19). Therefore, a better comprehension of the regulatory mechanism of RLRs-mediated IFNs in tumor immunity is of great clinical importance for patients with bladder cancer.

Tremendous efforts have recently been dedicated to the investigation of metabolic reprogramming in the regulation of tumor immunity (20-22). Among them, amino acid metabolism has attracted widespread attention. Asparagine synthetase (ASNS) catalyzes the conversion of aspartate to asparagine in an ATP-dependent reaction. Currently, L-asparaginase (ASNase), a drug that deprives plasma asparagine, is considered to be a first-line therapy for childhood acute lymphoblastic leukemia (ALL) (23). Accumulating studies have revealed that asparagine is tightly linked to the activation and differentiation of CD8+ T cells, thereby affecting antitumoral functionality (24-26). In addition, ASNS is always elevated in many cancer types and increased asparagine contributes to cancer cell survival and metastasis (27-29). Nonetheless, the specific roles of asparagine metabolism on the cancer cell-intrinsic functions and on the regulation of RLRs-mediated antitumor immunity have not been explored.

Here, we report that asparagine restriction enhances RIG-I mediated IFNs signaling and potentiates antitumor immunity in bladder cancer. Clinically, ASNS is upregulated and is associated with a poor response to immunotherapy in bladder cancer. Limiting asparagine by knockdown of ASNS or treatment with ASNase increases intratumoral CD8+ T cells infiltration and effector function, thus boosting the efficacy of PD-1 blockade. Mechanistically, asparagine can directly facilitate the interaction between E3 ligase CBL and RIG-I, consequently inducing RIG-I degradation to suppress IFN signaling, thereby limiting antitumor immune responses. Our study highlights a role of asparagine in regulating RIG-I stability and connect asparagine metabolism to the IFN-I signaling that modulates antitumor immunity, suggesting that targeting ASNS is a promising approach to enhance immunotherapy for bladder cancer.

Results

Asparagine restriction attenuates tumor growth in an immunity-dependent manner

Previous study reports that ASNS function as a critical enzyme that catalyzes the biosynthesis of asparagine from aspartate in an ATP-dependent reaction (23). To interrogate the biological functions of ASNS on cancer cells, we knocked down the *Asns* gene in two malignant mouse bladder cancer cell lines (MB49 and MBT2) and a human bladder cancer cell lines UMUC3 (Supplemental Figure 1, A and B). To our surprise, loss of ASNS did not alter the in vitro growth rates and migration abilities of tumor cells (Supplemental Figure 1, C-F). Consistent with this, we found that asparagine also had no obvious difference on the proliferation abilities of bladder cancer cells compared with the control cells (Supplemental Figure 1G).

To investigate the effect of ASNS on tumor growth in vivo, ASNS-deficient mouse bladder cancer cells were injected subcutaneously into the flanks of immunocompromised mice. Our results demonstrated that loss of ASNS had no effect on tumor growth in BALB/c nude mice (Figure 1, A and B, and Supplemental Figure 1, H and I). To determine the involvement of the immune system, we inoculated ASNS-deficient and control bladder cancer cells into syngeneic mice hosts. Of note, silencing of ASNS inhibited tumor growth in both immunocompetent mice (Figure 1, C and D). To assess the effect of asparagine on the tumor growth in vivo, we subcutaneously injected murine bladder cancer cells into mice, and followed by oral administration of PBS or asparagine, respectively. We observed no significant difference in immunocompromised mice administrated with asparagine (Figure 1, E and F). However, asparagine treatment promoted tumor growth in both immunocompetent murine bladder cancer models (Figure 1, G and H). Collectively, these data suggest that asparagine restriction could suppress tumor growth, which requires the presence of an intact immune system.

Knockdown of ASNS potentiates recruitment and activation of CD8+ T cells

We next attempted to quantify immune effector cells in control and ASNS-deficient bladder tumors by flow cytometry. Gating strategy to analyze the population of immune

cells in mouse transplanted tumors was shown in Supplemental Figure 2A. We found that knockdown of ASNS could significantly increase CD8+ T cells infiltration in both tumors established by MB49 and MBT2 cells (Figure 2A). However, there were no consistent differences in CD4+ T cells and NK cells in both models (Supplemental Figure 3, A-D). Previous studies have shown that T cells exclusion from the tumor parenchyma is one of the mechanisms underlying immunosuppression in the TME and is associated with poor response to current immunotherapies (30, 31). Notably, depletion of ASNS also increased the infiltration of CD8+ T cells in tumor parenchyma (Figure 2B) and enhanced their cytokines production including GZMB, TNF-α and IFN-γ (Figure 2, C and D, and Supplemental Figure 2B). On the contrary, asparagine treatment decreased the infiltration of CD8+ T cells and impaired function of CD8+ T cells to secrete GZMB (Figure 2, E and F, and Supplemental Figure 3E).

To determine the extent to which ASNS inhibition promoted an antitumor reaction dependent on $CD8^+$ T cells in vivo, CD8+ T cells were deleted using anti-CD8 antibody (Figure 2G and Supplemental Figure 3, F and G). We found that ASNS deficiency-mediated antitumor function was largely abolished in the CD8+ T cell-depleted group (Figure 2, H and I). Collectively, these results indicate that the tumor-suppressive effect of asparagine restriction might be mediated by tumor-infiltrating CD8+ T cells.

Silencing of ASNS triggers RIG-I-induced type I IFN signaling

To further decipher the mechanism of immunoactivation mediated by ASNS inhibition, we performed RNA-sequencing analysis in ASNS-deficient MBT2 cells (Figure 3A and Supplemental Figure 4A). Gene ontology (GO) analysis and gene set enrichment analysis (GSEA) showed that differentially expressed genes were enriched in biological pathways related with IFN pathway and adaptive immune response process, including response to type I IFN, regulation of T cell mediated cytotoxicity and so on (Figure 3, B and C, and Supplemental Figure 4B). Then, we confirmed the RNA-seq data that knockdown of ASNS elevated the expression of interferon-stimulated genes (ISGs)

(e.g., OAS2, OAS3, RIG-I, CCL5 and ISG15) and IFN-β (Figure 3D and Supplemental Figure 4C). We also applied Luminex system multiple immunoassays to detect multiple cytokines and chemokines in cell culture supernatants from ASNS-deficient and control MBT2 cells. Supporting the results obtained in RNA-seq, knockdown of ASNS upregulated the expression of CCL5 and promoted its secretion (Figure 3E), which is robustly correlated with CD8+ T cells infiltration in solid tumors (32). Moreover, the secretion levels of IFN-β and CCL5 protein were improved in ASNS-deficient bladder cancer cells by using ELISA (Figure 3F and Supplemental Figure 4D). In contrast, asparagine attenuated the expression of IFN-β and CCL5 in bladder cancer cells (Supplemental Figure 4, E and F).

Previous studies have reported that several innate sensing pathways can stimulate the induction of type I IFNs. For example, cGAS-STING of dsDNA sensors, RIG-I/MDA5-MAVS of dsRNA sensors and Toll-like receptors (TLR3 and TLR4) of LPS sensors converge at the activation of TANK-binding kinase 1 (TBK1) and interferon regulatory factor 3 (IRF3), trigging the expression of type I IFNs (33). However, type I IFNs mediated by intracellular nucleic acid sensors are a key component to activate the immune system against cancer (34). Therefore, we inhibited the expression of pivotal nucleic acid sensors by shRNA-mediated silencing prior to knocking down ASNS to identify which sensor was essential for ASNS inhibition induced IFN-I activation. Intriguingly, abrogation of MAVS (Figure 3G), but not STING (Supplemental Figure 4G), substantially diminished the induction of IFN-β in response to ASNS inhibition. Therefore, we speculated that RIG-I/MDA5-MAVS pathway was essential for IFN-I activation upon ASNS inhibition. Then, we confirmed that knockdown of ASNS was sufficient to enhance IFN-β and CCL5 production following transfection of dsRNA mimic analogue poly (I:C) (Figure 3, H and I, and Supplemental Figure 4H), a synthetic dsRNA analogue (35). Conversely, exogenous asparagine decreased the expression of IFN-β and CCL5 induced by poly(I:C) (Figure 3J and Supplemental Figure 4, I and J). Previous study has been reported that L-asparaginase (ASNase) is a core component of

the chemotherapy regimen for childhood acute lymphoblastic leukemia, which could participate in the catabolism of asparagine (36). Notably, the expression levels of IFN-β and CCL5 were higher in bladder cancer cells treated with ASNase (Figure 3K and Supplemental Figure 4K).

Giving that endogenous dsRNAs is responsible for activating the cytoplasmic dsRNA sensors and triggering IFN-I response in several types of cancer cells (37, 38). We investigated the level of endogenous dsRNAs using a dsRNA-specific antibody and found that the depletion of ASNS substantially had no obvious effect on the level of endogenous dsRNA (Supplemental Figure 5A). Of note, knockdown of ASNS or asparagine could alter the expression of IFN-β and CCL5 upon poly(I:C) treatment. We speculated that ASNS loss or asparagine exerted their function by mediating dsRNA sensors, but not dsRNA production. To further explored whether ASNS inhibition activated RIG-I/MDA5 signaling and we found that knockdown of ASNS upregulated RIG-I expression and promoted the phosphorylation of IRF3 proteins, a transcription factor that induces IFN expression (Figure 3L and Supplemental Figure 5B). We also observed a reduction of the RIG-I expression under asparagine addition (Supplemental Figure 5C), but not aspartate (Supplemental Figure 5D). In addition, we demonstrated that poly (I:C) intensely increased the expression of RIG-I and p-IRF3 protein, which could be reduced by asparagine in bladder cancer cells (Figure 3M and Supplemental Figure 5E). Importantly, the upregulation of RIG-I and p-IRF3 protein levels induced by ASNS knockdown was considerably abolished by asparagine (Figure 3N and Supplemental Figure 5F). Collectively, these findings reveal that ASNS inhibition could activate RIG-I-induced IFN-β signaling in bladder cancer.

To further investigate whether IFN-β signaling is essential for ASNS inhibition-elicited antitumor immunity, we genetically abrogated IFN-β production in bladder cancer cells (Supplemental Figure 6A), which completely reversed ASNS deficiency-mediated inhibition of tumor growth in vivo (Figure 3, O and P, and Supplemental

Figure 6, B and C). In line with this, we blocked IFN-β signaling using anti-IFNAR1 antibody in vivo and also found that treatment with anti-IFNAR1 antibody markedly restored the growth retardation of ASNS-deficient tumors in C57BL/6 mice (Supplemental Figure 6, D-G). Taken together, these results strongly indicate that IFN-β signaling plays a pivotal role in ASNS deficiency-mediated antitumor immune responses.

Cellular asparagine abundance affects RIG-I protein stability

We next sought to investigate the mechanism involved in ASNS inhibition-induced IFN-I pathway activation. The aforementioned results have depicted that ASNS inhibition could elevate the expression levels of mRNA and protein of RIG-I. Of note, previous studies have reported that RIG-I, as a ISGs, could be strongly induced by IFNs in a positive feedback manner (39, 40). Therefore, we inhibited the expression of MAVS by shRNA before knocking down ASNS to block the feedback effect of the IFN-I signaling on RIG-I, and found that knockdown of ASNS upregulated the expression of RIG-I protein, but not mRNA (Figure 4, A and B). Consistently, asparagine only decreased the level of RIG-I protein (Figure 4, C and D). Then, we transfected Flag-RIG-I plasmids in HEK293T cells and found that asparagine treatment attenuated the RIG-I and IFN-β expression (Figure 4E). Therefore, we hypothesized that RIG-I upregulation induced by ASNS inhibition was achieved by monitoring its protein layer.

Subsequently, we conducted CHX experiment and found that silencing of ASNS significantly extended the half-life of RIG-I protein, indicating that ASNS knockdown inhibited the degradation of RIG-I (Figure 4, F-I). In addition, the reduction of RIG-I protein induced by asparagine was abolished by proteasome inhibitor MG132 in bladder cancer cells, but not lysosome inhibitor CQ (Figure 4, J and K). Co-immunoprecipitation experiments indicated that asparagine markedly increased K48-linked ubiquitination of RIG-I (Figure 4L), whereas ASNS deficiency decreased K48-linked ubiquitination of RIG-I (Figure 4M). Collectively, these data suggest that

knockdown of ASNS upregulates RIG-I expression by protecting it from degradation.

Asparagine binds to RIG-I and enhances its ubiquitination by CBL

Increasing evidences indicate that the E3 ubiquitin ligases RNF122, RNF125, STUB1 and CBL play pivotal role in the RIG-I degradation via K48-linked ubiquitination (19, 41). We further determined how asparagine affects K48-linked polyubiquitination and suppression of RIG-I. Co-immunoprecipitation experiments indicated that asparagine promoted the association of CBL with RIG-I but not RNF122, RNF125, and STUB1 in mammalian overexpression system (Figure 5A and Supplemental Figure 7, A-C). Importantly, we demonstrated that asparagine could promote the polyubiquitination of RIG-I protein in CBL-overexpressed cells (Figure 5B). In contrast, CBL knockdown ablated the promotion of RIG-I polyubiquitination elicited by asparagine (Supplemental Figure 7D). Even though asparagine may trigger certain metabolic processes that can influence CBL-mediated RIG-I ubiquitination, it is attractive to detect whether asparagine acts directly on RIG-I. We thus tested the effect of asparagine on CBL-mediated ubiquitination of RIG-I in vitro. In the presence of E1, E2, ATP and Ub, CBL promoted RIG-I ubiquitination, and asparagine addition strikingly enhanced ubiquitination (Figure 5C). Notably, microscale thermophoresis (MST) assay, an in vitro assay for direct interaction between proteins and small molecules, revealed that asparagine had a high affinity to bind to RIG-I with a Kd of 303 μM (Figure 5D), but did not show any affinity to CBL (Figure 5E). Thus, these results indicated that asparagine could directly bind to RIG-I and promote its degradation. We further observed that asparagine mediated reduction of the RIG-I and p-IRF3 (Figure 5F and Supplemental Figure 7, E and F) as well as downregulation of IFN-β and CCL5 (Figure 5G and Supplemental Figure 7, G and H) were partially rescued by CBL knockdown.

Then, we detected the function of CBL knockdown on tumor growth and CD8+ T cell infiltration. The results revealed that silencing of CBL partially rescued the promotion of tumor growth and reduction of CD8+ T cells infiltration caused by

asparagine (Supplemental Figure 7, I-L). Furthermore, we found that loss of RIG-I significantly increased the size of tumors derived from bladder cancer cells depleted ASNS (Figure 5H). ASNS deficiency resulted in an obvious increase in infiltration of CD8+ T cells, which was attenuated by RIG-I knockdown (Figure 5I). Taken together, these data indicate that asparagine promotes the K48-linked ubiquitination of RIG-I by CBL, thereby attenuating antitumor immune response.

Asparagine restriction sensitizes tumors to PD-1 blockade

Tumor mutation burden has been proposed as a predictive biomarker for response to ICIs (42). Based on the high mutation profiles of bladder cancer, we therefore explored the therapeutic effect of PD-1 blockade monotherapy in vivo. We found that PD-1 blockade alone had minimal effect on tumor growth delaying effect (Supplemental Figure 8, A-D), consistent with previous report (43). Thus, it is necessary to improve the efficacy of ICIs by developing combination therapies.

Considering that ASNS inhibition could enhance CD8+ T cells infiltration and promote its activation, we further explored whether ASNS could affect the efficacy of anti-PD-1 treatment preclinically. We conducted tumor growth experiments with anti-PD-1 antibody in syngeneic mice inoculated with ASNS-deficient MB49 tumor cells. Our results demonstrated that anti-PD-1 antibody synergized with ASNS deficiency in suppressing tumor growth (Figure 6A). Flow cytometry analysis also showed that ASNS knockdown combination with anti-PD-1 treatment significantly increased the infiltration of CD8+ T cells (Figure 6B). More importantly, ASNase markedly enhanced the antitumor effects of PD-1 blockade in the subcutaneous tumor models established by MB49 cells (Figure 6, C-E). Further analysis of immune infiltration revealed that combination treatment could also promote CD8+ T cells infiltration (Figure 6F). In addition, there was no obvious difference in body weight among the four groups of mice (Figure 6G). Consistent with the observations made in MB49 tumor mice, a notable delay in tumor growth was observed in MBT2 tumor mice treated with the

ASNase and PD-1 blockade (Figure 6H and Supplemental Figure 8, E and F). Furthermore, in terms of that the subcutaneous model does not faithfully recapitulate the microenvironment of bladder cancer, we applied the orthotopic bladder tumor model along with ASNase and anti-PD-1 treatment. As shown in Figure 6I-J, ASNase alone reduced tumor growth, and the combination of anti-PD-1 and ASNase more efficiently suppressed tumor progression. Immunofluorescence staining results indicated that anti-PD-1 antibody increased CD8+ T cells number infiltrated in tumors, which could be strengthened upon ASNase treatment (Figure 6J). Altogether, these results indicate a potent synergy between ASNS inhibition and PD-1 blockade in controlling tumor growth in bladder cancer.

Upregulated ASNS leads to immunotherapy resistance in bladder cancer

To further explore the profiles of ASNS in bladder cancer, we mined the TCGA dataset and found that the mRNA level of ASNS was significantly upregulated in bladder cancer (Figure 7A). We then confirmed that the level of ASNS protein was higher in bladder cancer tissues than that in paired normal bladder tissues (Figure 7B). Moreover, Immunohistochemical (IHC) staining in bladder cancer tissues array showing the expression of ASNS was upregulated in tumor tissues (Figure 7C). Further Kaplan-Meier analysis revealed that high expression of ASNS was associated with poor overall survival for bladder cancer patients (Figure 7D). Next, we verified the correlation between tumor ASNS, RIG-I, and CD8 expression in tissues of patients with cancer. IHC staining exhibited a negative correlation between tumor CD8 expression and ASNS expression in human bladder cancer clinical samples (Figure 7, E and F). Similar to CD8, we found that tumor RIG-I expression was also inversely correlated with ASNS protein expression (Supplemental Figure 9A). Furthermore, the infiltration degree of CD8+ T cells showed a remarkable positive correlation with RIG-I (Supplemental Figure 9B).

To further assess the clinical value of ASNS in ICIs therapy, we analyzed

immunotherapy cohort containing 57 bladder cancer patients treated with ICIs from our hospital (301-immune cohort). The expression of ASNS at baseline was lower in responders to ICIs compared with non-responders (Figure 7, G and H, and Supplemental Figure 9C). Meanwhile, low levels of ASNS expression were associated with improved progression-free survival in these patients (Figure 7I). Moreover, multi-color IF images confirmed a negative correlation between ASNS expression and RIG-I expression, CD8+ T cells infiltration (Figure 7J), revealing the mechanism of response or non-response to ICIs treatment. Thus, these data indicated that ASNS could be a predictive biomarker for bladder cancer ICIs therapy.

Discussion

Recently, ICIs therapy has become a promising therapeutic strategy with bladder cancer due to its high levels of mutational burden (2). However, only a minority of patients benefit from this strategy while a considerable proportion of patients either fail to respond or progress rapidly to resistance after initial response (8). Therefore, finding predictive biomarkers for increasing immune response and developing therapeutic strategies to potentiate immunotherapy efficacy are urgently needed. Our study found that ASNS expression is a predictive biomarker for immunotherapy response in bladder cancer, and FDA-approved ASNase dramatically boosts the antitumor efficacy of anti-PD-1 therapy. Anti-PD-1 therapy combined with ASNase in advanced bladder cancer is worthy to investigate in future clinical trials. Previous studies showed that asparagine availability favors tumor cell proliferation, metastasis and survival ability in various types of cancers (27-29), while we found that knockdown of ASNS or asparagine addition had no obvious effect on proliferation or migration of bladder cancer cells, indicating cancer type-specific functions in asparagine metabolism. However, further research should focus on the underlying mechanisms of ASNS upregulation in bladder cancer, which may help to advance understanding its special role.

Modulation of amino acid metabolism has emerged as a way to reprogram the

tumor microenvironment and has shown great promise for cancer treatment, but major studies have focused on immune cells themselves so far (20-22, 44, 45). As a nonessential amino acid, asparagine uptake and biosynthesis enable CD8+ T cells activation (early phase) (24-26), while exerting opposing effects during differentiation (late phase) (26). These studies revealed asparagine as a critical metabolic node to shape T cell effector functions and antitumor responses. However, it is unclear whether asparagine has any effect on tumor-intrinsic functions to regulate immune responses. Our data demonstrate that limiting asparagine by knockdown of ASNS or treatment with ASNase in bladder cancer facilitates RIG-I mediated IFN-I signaling, promoting the intratumoral CD8+ T cells infiltration and PD-1 blockade efficacy. Together, these encouraging results imply that remodeling of asparagine metabolism is critical for relieving tumor-mediated immunosuppression and effective way to enhance antitumor immunity.

Increasing evidences indicate that the exclusion of CD8+ T cells in TME is associated with poor response to immunotherapy (30, 31). Herein, we demonstrated that knockdown of ASNS could potentiate recruitment and activation of CD8+ T cells in bladder cancer. However, ASNS deficiency-mediated antitumor responses was not completely reversed by CD8 depletion in syngeneic mice. In contrast, depletion of IFN-β and anti-IFNAR1 antibody treatment almost completely reversed tumor regression mediated by ASNS knockdown in syngeneic mice, suggesting that other types of immune cells besides CD8+ T cells might also contribute to ASNS loss-triggered antitumor immunity. Previous studies have shown that cytotoxic CD4+ T cells and NK cells could mediate the antitumor responses of bladder cancer (46, 47). We hypothesized that although silencing of ASNS showed no obvious difference in the number of CD4+ T cells and NK cells in TME, it may alter their status and function.

Post-translational modification of the RLRs directly regulates their expression and activity, subsequently modulating the downstream IFN-I signaling (48, 49). Of note,

K48-linked ubiquitylation catalyzed by several E3 ligases, such as RNF122, RNF125, CBL or STUB1, contributes to the degradation of RIG-I, thereby influencing pathway activation (41, 50-52). By far, little is known about whether nutrient metabolite is crucially involved in the regulation of RIG-I-IFN signaling. In this study, we identify asparagine as a metabolic regulator of RIG-1 stability and verify that asparagine directly binds to RIG-I, promoting CBL-mediated polyubiquitination and proteasomal degradation of RIG-I. Previous studies report the metabolism-independent role for asparagine in the direct modulation of LKB1 and LCK kinase activity (24, 29). We uncover that asparagine could be an endogenous metabolite binding to RIG-I and regulate its stability. However, further structural study may be required to comprehensively understand how asparagine acts on RIG-I-CBL complex.

In conclusion, our study establishes a critical role of asparagine in limiting type I IFN signaling and identifies RIG-I as a direct sensor of asparagine, which furnishes a rationale for future clinical applications of the combinatorial use of ASNase and ICIs in bladder cancer.

Methods

Sex as a biological variable. Male and female human bladder cancer samples were analyzed. Male and female mice were used in all mouse studies. In this study, sex was not considered as a biological variable.

Animals. Six- to eight-week-old C3H mice were purchased by Beijing Vital River Laboratory Animal Technology Co., Ltd (Beijing, China). C57BL/6 mice and BALB/c nude mice aged 6-8 weeks were purchased from GemPharmatech Co., Ltd (Nanjing, China). All mice were maintained at room temperature with free access to food and water with a 12-h light/dark cycle in a barrier facility.

Cell lines and clinical samples. The bladder cancer cell lines UMUC3 were

obtained from the ATCC. HEK293T cells were also purchased from the ATCC. The murine malignant bladder cell lines MB49 and MBT2 were purchased from Meisen CTCC (Zhe jiang, China). The UMUC3, MB49 and MBT2 cells were cultured in DMEM (Procell, China). All the medium were supplemented with 10% FBS (Procell, China), 1% penicillin and streptomycin (Procell, China). The condition of incubator was set as 37°C with 5% CO_2. All cell lines were routinely confirmed negative for *Mycoplasma* contamination. Resected human bladder cancer tissues and their corresponding clinical information were acquired from the Department of Urology of the Chinese PLA General Hospital. The histologic and pathologic type of all tissues were confirmed by three experienced pathologists independently. For the 301-immune cohort, a total of 57 bladder cancer patients receiving ICIs were included from Chinese PLA General Hospital (301). ICIs treatment efficacy was inspected by at least 3 pathologists based on the Response Evaluation Criteria in Solid Tumors (RECIST). The samples were obtained with written informed consent of all patients before the research started.

Plasmids construction and transfection. Short hairpin RNA sequences against mouse Asns, Rig-i, Mavs, c-Cbl and human ASNS were synthesized by Biomed (Beijing, China), and were cloned into the pLKO.1 vector. Knockdown plasmid against mouse Sting has been constructed in our previous study (53). The overexpression vector of RIG-I was kindly gifted from Weina Zhang (Academy of Military Medical Sciences, Beijing, China). The human RNF122, RNF125, STUB1 and CBL cDNA were synthesized by Biomed, which were cloned into pCMV-HA vector to construct overexpression plasmid. SgRNA sequence of Ifnb was synthesized by Biomed (Beijing, China), and was cloned into the lentiCRISPR v2 vector. The lentiviral vectors were transfected in HEK293T cells with the PAX2 and VSVG packaging plasmid. After 48 h or 72 h transfection, supernatants were collected and concentrated with Lentivirus Concentration Reagent (GenStar, China) for overnight in 4℃. To construct the stably transfected cell lines, cells were infected with relative lentiviruses for 24 h, then were

screened with puromycin for 1 weeks. shRNA sequences are also listed in Supplemental Table1.

Cell viability assays. For the cell proliferation assay, the bladder cancer cells were seeded in 96-well plates in 100 μl complete culture media for various time periods (2000 cells per well). Cell Counting Kit-8 assay (Dojindo, Japan) was performed to measure cell viability according to the manufacturer's instructions.

Animal experiments. For the subcutaneous tumorigenesis experiments, 6- to 8-week-old BALB/c nude mice, C57BL/6 and C3H mice were used. MB49 (5×10^5 per mouse) and MBT2 (1×10^6 per mouse) cells stably transfected with the pLKO.1-shAsns#1 plasmid or pLKO.1-Vector plasmid were subcutaneously injected into the right flank of each mouse. When a tumor was palpable, it was measured using a caliper every 3-4 days, and its volume was calculated according to the formula volume = length × width^2 × 0.5. Four days after implantation, mice were treated with 100μg of either control IgG2α (Bioxcell, BE0085, USA) or anti-PD-1 antibody (Bioxcell, BE0146, USA). The drugs were administered twice a week for 3 weeks. For Asparagine experiment, mice were fed with drinking water containing with or without 10mM Asparagine (Solarbio, China). For drug combination experiments, 5-week-old C57BL/6 or C3H mice were inoculated subcutaneously with MB49 cells (5×10^5 per mouse) or MBT2 cells (1×10^6 per mouse), respectively. Next, mice received treatment i.p. with vehicle or ASNase (2 U per g) (ProSpec, Israel) three times a week for 3 weeks. In addition, 100 μg of anti-PD-1 antibody were injected on days 5 twice a week for 3 weeks in combination with the ASNase. For neutralization of IFNAR1, tumor-bearing mice were injected i.p. with 200μg/mouse anti-IFNAR1 (BioXcell, BE0241, USA) at on days 0, 7, 14 and 21.

Quantitative real-time PCR. Briefly, total RNA was isolated from bladder cancer cells in each condition using FastPure Cell/Tissue Total RNA Isolation Kit V2 (Vazyme,

China) according to the manufacturer's instructions. RNA of each sample was complementarily reversed to cDNA by HiScript III RT SuperMix for qPCR (Vazyme, China). cDNA product of each sample was used as template to conduct quantitative PCR by ChamQ Universal SYBR qPCR Master Mix (Vazyme, China). Quantitative RT-PCR was performed using CFX96 Real-Time PCR System (Bio-Rad, USA). The fold changes of gene expression were calculated after being normalized to 18s or ACTB. The primer pairs used in this study were listed in Supplemental Table1.

Western blotting analysis. Briefly, cells were lysed by using RIPA buffer containing proteinase inhibitors cocktail and PMSF on ice for 30 min. Protein samples were quantified using BCA protein assay kit (Solarbio, China) and boiled in 5 × loading buffer for 10 min at 95°C. Protein lysates were resolved by SDS-PAGE and transferred onto polyvinyldifluoride (PVDF) membrane. Then, the membranes were blocked by 5% skimmed milk and probed with primary antibodies against Actin (bioeasytech, BE0033, China), Asns (Proteintech, 14681-1-AP, USA), Sting (Proteintech, 19851-1-AP, USA), Mavs (Proteintech, 14341-1-AP, USA), Rig-i (CST, 4200, USA), Mda5 (ABclonal, A2419, China), Irf3 (CST, 4302, USA), p-Irf3 (CST, 29047, USA) and CBL (Proteintech, 25818-1-AP, USA) at 4°C overnight. Membranes were washed with TBST for three times and then incubated with HRP-conjugated anti-rabbit (Proteintech, SA00001-2, USA) or anti-mouse (Proteintech, SA00001-1, USA) secondary antibodies at room temperature for 1 h. Finally, the protein bands were visualized using ECL substrate kit via QuickChemi 5200 Imaging System.

Migration assays. For migration assays, approximately 4×10^4 cells in 200 μL serum-free culture media were seeded in the upper chamber of 24-well Transwell chamber system. About 600 μL culture media with 10% FBS were added to the lower chamber. After incubation for 24 h, cells were fixed in paraformaldehyde for 15 min and then stained with 0.1% crystal violet for 30 min. The migrated cells were counted in three randomly selected fields.

FACS analysis with tumor-infiltrating immune cells. Mice harboring tumors were collected after inoculation, weighed, and mechanically minced and digested in DNase I and collagenase IV (Sigma, USA) for 60 min at 37°C. The dissociated cells were filtered by 70 μm cell strainers (BIOFIL, China) to obtain single cell suspension for flow cytometry analysis. Tumor cells were washed with RPMI-1640 medium and lysed with RBC Lysis Solution (Beyotime, China). Then, BV510 anti-mouse CD45 (BioLegend, 103137, USA), BV605 anti-mouse CD3 (BioLegend, 100237, USA), Alexa Fluor® 488 anti-mouse CD4 (BioLegend, 100423, USA), APC/Fire™ 750 anti-mouse CD8a (BioLegend, 100766, USA) and APC-mouse NK1.1 (BioLegend, 108710, USA) were used to stain cell members for 30 min in the dark. Flow cytometer was applied to detect stained cells, and FlowJo software was used to analyze the data.

For cytokine staining, tumor cells are digested into single cell suspension and centrifuged for 5 min at 1500 rpm. All cells were then cultured in 1640 medium (RPMI-1640 with 10% FBS and penicillin/streptomycin) with GolgiPlug (BD, 554724, USA) and eBioscience™ (Thermo Fisher Scientific, 00-4970-93, USA) for 3 h at 37 °C. Cells were washed and live/dead staining (Thermo Fisher Scientific, 65-0865-14) and BV421 anti-mouse CD45 (BioLegend, 103133, USA) and PerCP anti-mouse CD8 (BioLegend, 100731, USA) staining were performed. Then cells were fixed for 1 h at room temperature in Fixation/ Permeabilization Concentrate and washed in permeabilization buffer (Thermo Fisher Scientific, 00-5523-00, USA). APC anti-mouse TNFα (BioLegend, 506307, USA) and PE anti-mouse IFNγ (BD, 554412, USA) staining was performed in permeabilization buffer at room temperature for 30 mins. Cells were washed and resuspended in FACS buffer for analysis on flow cytometer.

Immunohistochemical staining. Paraffin-embedded tissues were sectioned and used to detect the expression of ASNS, RIG-I and CD8. IHC staining was conducted as described previously. Briefly, samples were incubated with primary antibodies, including anti-ASNS (proteintech, 14681-1-AP, USA), anti-RIG-I (ABclonal, A21421,

552 China) and anti-mCD8a (CST, 98941, USA) at 4°C overnight. Sections were incubated
553 with enzyme-conjugated secondary antibody followed by washing three times with
554 PBS. After washing, sections were incubated with DAB substrate kit. Sections were
555 counterstained with hematoxylin. The stained bladder cancer tissues were scored based
556 on a scoring method as follows: staining intensity was scored 0 (negative), 1 (low), 2
557 (moderate), and 3 (high). Staining range was scored 0 (0% stained), 1 (1%-25% stained),
558 2 (26%-50% stained), and 3 (51%- 100% stained). The total score was calculated
559 according to the formula score = intensity score × percentage score.
560
561 *Immunofluorescence.* For dsRNAs immunofluorescence, cells were plated on
562 glass coverslips in 24-well. After overnight cultivation, cells were washed three times
563 with PBS and then fixed with 4% formaldehyde at room temperature for 20 minutes
564 and permeabilized with 0.5% Triton-X100 in PBS for 5 minutes at room temperature.
565 Then, cells were blocked by 1% BSA and incubated in the J2 antibody (SCICONS,
566 10010200, Hungary) at 4°C overnight. The following day, cells were washed three
567 times with PBST and incubated with ABflo® 594-conjugated Goat anti-Mouse IgG
568 (ABclonal, AS054, China) for 1 h at room temperature, followed sealing with antifade
569 mounting medium containing DAPI.
570
571 For multiplex immunofluorescence staining of tissues, tumors were captured and
572 fixed in 10% formalin overnight and embedded in paraffin. The embedded tissues were
573 sectioned into slices with a thickness of 4 μm, deparaffinized and hydrated, antigen
574 retrieved in 10 mmol/L sodium citrate for 20 mins in a microwave oven and cooling to
575 room temperature slowly. Sections were permeabilized with 0.5% Triton X-100 in PBS
576 for 5 mins and then blocked with 2% BSA in PBS for 1 h at room temperature. The
577 sections were incubated with anti-mCD8a (CST, 98941, USA), anti-GZMB
578 (proteintech, 13588-1-AP, USA), anti-hCD8a (CST, 70306, USA), ASNS (proteintech,
579 14681-1-AP, USA) and anti-RIG-I (ABclonal, A21421, China) overnight at 4°C.
580 Subsequently, sections were washed with PBS and incubated with fluorescein-

conjugated secondary antibody at room temperature for 1 h. After incubation with DAPI, the slides were imaged and visualized using CLSM 600 confocal laser scanning microscope (Sunnysoptop, China).

In vivo experiments with CD8 depletion. MB49 (5×10^5 per mouse) and MBT2 (1×10^6 per mouse) cells stably transfected with the pLKO.1-shAsns#1 plasmid, pLKO.1-shAsns#2 plasmid or pLKO.1-Vector plasmid were subcutaneously injected into 6- to 8-week-old C57BL/6 mice and C3H mice, respectively. To evaluate the role of CD8+ T cells in mice, the 200 μg of anti-CD8a antibody (MCE, HY-P99129, USA) was injected intraperitoneally on days -3, 0, 3, 8 and 11. Equal amounts of IgG isotype antibodies were injected as a control. Tumor volume and growth curve were detected as mentioned above.

RNA-seq and Gene Set Enrichment Analysis (GSEA). Total RNA isolated using FastPure Cell/Tissue Total RNA Isolation Kit V2 (Vazyme, China). RNA-seq analysis was performed by Majorbio Bio-pharm Technology Co., Ltd (Shanghai, China). Transcriptome library was prepared following TruSeq RNA sample preparation Kit from Illumina (San Diego, CA) using 1 μg of total RNA. DEGs with $|\log2FC| > 1.5$ and *P* adjust value ≤ 0.05 were considered to be significantly different expressed genes. The data were analyzed on the online platform of Majorbio Cloud Platform. Sequencing results were deposited in the Gene Expression Omnibus database (GSE270353) with accession number ejsjswsgdhupzqj. GSEA algorithm was used to analyze the biological functions of the genes based on type I IFN-related molecular signatures collected from Molecular Signatures Database (MSigDB).

Luminex liquid suspension biochip detection. MBT2 cells stably transfected with the pLKO.1-shAsns#1 plasmid or pLKO.1-Vector plasmid were cultured in the 6-well plates. After 24 h, cell culture supernatants were collected, and the inflammatory cytokines and chemokines were detected (including: CCL1, CCL2, CCL3, CCL4,

CCL5, CCL7, CCL11, CCL12, CCL17, CCL19, CCL20, CCL22, CCL24, CCL27, CXCL1, CXCL5, CXCL10, CXCL11, CXCL12, CXCL13, CXCL16, CX3CL1, IL-2, IL-4, IL-6, IL-10, IL-16, GM-CSF, IFN-γ, IL-1β, TNF-α) by a Luminex protein biochip testing system (Wayen Biotechnologies, Shanghai, China) according to manufacturer's instruction. The data were measured and collected by the Luminex 200 system. The results were showed in supplemental Table2.

ELISA. Cell culture supernatants were collected from 6-well plates, and the presence of the cytokine/chemokine proteins was determined using the Mouse IFN-β and Mouse CCL5 ELISA kit (Elabscience, USA) according to the manufacturer's instructions. The concentrations of different cytokine/chemokine proteins were calculated based on OD values at a detection wavelength of 450 nm.

Co-IP. HEK293T cells were transfected with Flag-RIG-I and HA-RNF122, HA-RNF125, HA-STUB1 and HA-CBL together with Asparagine (Solarbio, China) for 42 h and cultured in medium containing MG132 (MCE, USA) for a further 6 h before co-immunoprecipitation. Then the cells were lysed with NP-40 buffer plus complete protease inhibitors PMSF and cocktail, and samples were cleaved on ice for 30 min. The lysates were centrifuged at 12,000 rpm for 10 min at 4°C. About 5-10% of the supernatants were used as input group, and the remaining samples were divided equally into IgG group and Flag group. The protein A/G beads were added in IgG or Flag antibodies at 4°C for 2h. Then the supernatants were incubated with antibodies-beads mix at 4°C overnight. Proteins interacting with beads were eluted off by re-suspending the beads in 1× SDS-PAGE loading buffer followed by heating at 95°C for 10 min. Proteins were separated by SDS-PAGE, followed by immunoblotting analysis with the Flag (proteintech, 66008-4-Ig, USA), HA (proteintech, 51064-2-AP, USA) and Ub-K48 (ABclonal, A3606, China) antibodies.

In vitro ubiquitination assay. Flag-RIG-I and HA-CBL were expressed in

HEK293T cells and purified using Flag and HA beads, respectively. The reaction was carried out at 37 °C for 2 h in 20 μl reaction buffer (40 mM Tris-HCl at pH 7.6, 2.5 mM Mg^{2+}-ATP, 2 mM dithiothreitol) containing the following components: 50 μM of ubiquitin, 100 nM E1, 1 μM E2, 2 μM HA-CBL, 5 μM Flag-RIG-I. The samples were stopped by adding SDS and boiled for 10 min, and then resolved by SDS-PAGE followed by immunoblot analysis using a monoclonal anti-Ub antibody.

Microscale thermophoresis (MST) assay. MST is a biomolecular interaction analysis technology that measures the affinity between a ligand and a target molecule (54). Briefly, the HEK293T cell lysate was collected after 48 h transfection with the Flag-RIG-I or HA-CBL plasmid. We purified Flag-tagged RIG-I and HA-tagged CBL by acid elution method. In total, 16 titration series of asparagine were prepared beginning at a concentration of 5mM and mixed with purified protein. All the samples were loaded into MST NT.115 standard glass capillaries and measurement was carried out using the MO. Control software.

Orthotopic bladder tumor model. An orthotopic bladder tumor mouse model was established as described previously (55) with minor modifications. In brief, under anesthesia, the C57BL/6 mice were placed in a supine position on a thermostatic blanket. Then, a 1-cm midline incision through the skin of the abdominopelvic region was made to locate the urinary bladder. Luc-labeling MB49 cells were resuspended with 50% Matrigel (Lablead, China) mixed with PBS (5×10^3 cells per mouse) and were injected into the bladder wall of mice using insulin syringe. The bladder was placed back inside while ensuring that all other organs were in their proper position. Mice were left for at least 5 days for tumor development. After tumor volume was measured by living image, mice were randomly allocated into four groups for ASNase or anti-PD-1 treatment. For bioluminescent imaging, mice were given 200 μL (15mg/ml) D-luciferin potassium salt (Lablead, China) intraperitoneally and imaged on a live imaging system (Berthold LB983, Germany).

Statistics. The results are presented as the mean ± SD. Kaplan-Meier method and log-rank test were used to calculate overall survival rates. The significance of intergroup differences was determined with 2-tailed Student's t-test, 1-way ANOVA or 2-way ANOVA. Statistical significance was assessed using GraphPad Prism software. A difference of $P < 0.05$ was considered statistically significant. *, $P < 0.05$; **, $P < 0.01$; and ***, $P < 0.005$ were defined.

Study approval. All bladder cancer tissue samples used in this study were obtained from patients with their informed consent, and the use of these samples was approved by the Institutional review board of the Chinese PLA General Hospital. All animal experiments were performed in accordance with institutional regulations and approval by the Institutional Animal Care and Use Committee of the Chinese PLA General Hospital.

Data availability. RNA-Seq data reported in this paper were deposited in the Gene Expression Omnibus (GEO) database (GSE270353) with accession number ejsjswsgdhupzqj. Values for all data points in graphs are reported in the Supporting Data Values file. All unique/stable reagents generated in this study are available from the corresponding author with a completed material transfer agreement.

Authors' Contributions

W. Wei: Conceptualization, data curation, formal analysis, investigation, methodology, writing-original draft. **H. Li:** Investigation, methodology. **S. Tian:** Formal analysis, validation, methodology. **C. Zhang:** Formal analysis, investigation. **J. Liu:** Formal analysis, investigation. **W. Tao:** Formal analysis, investigation. **T. Cai:** Investigation. **Y. Dong:** Investigation. **C. Wang:** Formal analysis. **D. Lu:** Investigation. **Y. Ai:** Resources. **W. Zhang:** Resources. **H. Wang:** Resources. **K. Liu:** Conceptualization, data curation. **Y. Fan:** Data curation. **Y. Gao:** Conceptualization, data curation, funding acquisition. **Q. Huang:** Conceptualization, data curation, funding acquisition. **X. Ma:**

Data curation, visualization. **B. Wang:** Conceptualization, data curation, funding acquisition. **X. Zhang:** Conceptualization, resources, supervision, funding acquisition. **Y. Huang:** Conceptualization, resources, data curation, formal analysis, supervision, funding acquisition, writing-original draft.

Acknowledgements

We thank Prof. Xin Pan and Prof. Weina Zhang for helpful discussions and advice for this project. We sincerely thank all patients in the study. We thank the Wayen Biotechnologies (Shanghai, China) for providing Luminex services. We also thank the Majorbio Company (Shanghai, China) for their enthusiastic support of this RNA-seq analysis. This study was supported by the grants from the National Natural Science Foundation of China (82103594 to Y. Huang, 82273412 to Q. Huang and 82372704 to B. Wang.), the National key research and development program (2022YFB4701700 to Y. Gao), the Youth Fund of Chinese PLA General Hospital (22QNCZ022 to Y. Huang) and the Minimally Invasive Innovation Team of the Urology Department of the Chinese PLA General Hospital (X. Zhang).

References

1. Sanli O, et al. Bladder cancer. *Nat Rev Dis Primers.* 2017;3:17022.
2. Alifrangis C, et al. Molecular and histopathology directed therapy for advanced bladder cancer. *Nat Rev Urol.* 2019;16(8):465-83.
3. Antoni S, et al. Bladder Cancer Incidence and Mortality: A Global Overview and Recent Trends. *Eur Urol.* 2017;71(1):96-108.
4. Patel VG, et al. Treatment of muscle-invasive and advanced bladder cancer in 2020. *CA Cancer J Clin.* 2020;70(5):404-23.
5. Patel MR, et al. Avelumab in metastatic urothelial carcinoma after platinum failure (JAVELIN Solid Tumor): pooled results from two expansion cohorts of an open-label, phase 1 trial. *Lancet Oncol.* 2018;19(1):51-64.
6. Sharma P, et al. Nivolumab in metastatic urothelial carcinoma after platinum therapy (CheckMate 275): a multicentre, single-arm, phase 2 trial. *Lancet Oncol.* 2017;18(3):312-22.
7. Felsenstein KM, and Theodorescu D. Precision medicine for urothelial bladder cancer: update on tumour genomics and immunotherapy. *Nat Rev Urol.* 2018;15(2):92-111.
8. Schneider AK, et al. The multifaceted immune regulation of bladder cancer. *Nat Rev Urol.* 2019;16(10):613-30.
9. Park J, et al. Microenvironment-driven metabolic adaptations guiding CD8(+) T cell anti-tumor

immunity. *Immunity.* 2023;56(1):32-42.
10. Chen DS, and Mellman I. Elements of cancer immunity and the cancer-immune set point. *Nature.* 2017;541(7637):321-30.
11. Schenkel JM, and Pauken KE. Localization, tissue biology and T cell state - implications for cancer immunotherapy. *Nat Rev Immunol.* 2023;23(12):807-23.
12. Chen Y, et al. CD8(+) T cell-based cancer immunotherapy. *J Transl Med.* 2024;22(1):394.
13. Gebhardt T, et al. Stem-like exhausted and memory CD8(+) T cells in cancer. *Nat Rev Cancer.* 2023;23(11):780-98.
14. Corrales L, et al. Innate immune signaling and regulation in cancer immunotherapy. *Cell Res.* 2017;27(1):96-108.
15. Yu R, et al. Type I interferon-mediated tumor immunity and its role in immunotherapy. *Cell Mol Life Sci.* 2022;79(3):191.
16. Heidegger S, et al. RIG-I activating immunostimulatory RNA boosts the efficacy of anticancer vaccines and synergizes with immune checkpoint blockade. *EBioMedicine.* 2019;41:146-55.
17. Gstalder C, et al. Inactivation of Fbxw7 Impairs dsRNA Sensing and Confers Resistance to PD-1 Blockade. *Cancer Discov.* 2020;10(9):1296-311.
18. Jiang Y, et al. Exploiting RIG-I-like receptor pathway for cancer immunotherapy. *J Hematol Oncol.* 2023;16(1):8.
19. Rehwinkel J, and Gack MU. RIG-I-like receptors: their regulation and roles in RNA sensing. *Nat Rev Immunol.* 2020;20(9):537-51.
20. Lemos H, et al. Immune control by amino acid catabolism during tumorigenesis and therapy. *Nat Rev Cancer.* 2019;19(3):162-75.
21. Yang L, et al. Amino acid metabolism in immune cells: essential regulators of the effector functions, and promising opportunities to enhance cancer immunotherapy. *J Hematol Oncol.* 2023;16(1):59.
22. Wang W, and Zou W. Amino Acids and Their Transporters in T Cell Immunity and Cancer Therapy. *Mol Cell.* 2020;80(3):384-95.
23. Richards NG, and Kilberg MS. Asparagine synthetase chemotherapy. *Annu Rev Biochem.* 2006;75:629-54.
24. Wu J, et al. Asparagine enhances LCK signalling to potentiate CD8(+) T-cell activation and anti-tumour responses. *Nat Cell Biol.* 2021;23(1):75-86.
25. Hope HC, et al. Coordination of asparagine uptake and asparagine synthetase expression modulates CD8+ T cell activation. *JCI Insight.* 2021;6(9).
26. Gnanaprakasam JNR, et al. Asparagine restriction enhances CD8(+) T cell metabolic fitness and antitumoral functionality through an NRF2-dependent stress response. *Nat Metab.* 2023;5(8):1423-39.
27. Gwinn DM, et al. Oncogenic KRAS Regulates Amino Acid Homeostasis and Asparagine Biosynthesis via ATF4 and Alters Sensitivity to L-Asparaginase. *Cancer Cell.* 2018;33(1):91-107.e6.
28. Knott SRV, et al. Asparagine bioavailability governs metastasis in a model of breast cancer. *Nature.* 2018;554(7692):378-81.
29. Deng L, et al. p53-mediated control of aspartate-asparagine homeostasis dictates LKB1 activity and modulates cell survival. *Nat Commun.* 2020;11(1):1755.
30. Joyce JA, and Fearon DT. T cell exclusion, immune privilege, and the tumor microenvironment.

Science. 2015;348(6230):74-80.
31. Park HR, et al. Angiopoietin-2-Dependent Spatial Vascular Destabilization Promotes T-cell Exclusion and Limits Immunotherapy in Melanoma. *Cancer Res.* 2023;83(12):1968-83.
32. Dangaj D, et al. Cooperation between Constitutive and Inducible Chemokines Enables T Cell Engraftment and Immune Attack in Solid Tumors. *Cancer Cell.* 2019;35(6):885-900.e10.
33. Zhao B, et al. Structural basis for concerted recruitment and activation of IRF-3 by innate immune adaptor proteins. *Proc Natl Acad Sci U S A.* 2016;113(24):E3403-12.
34. Zhuang Q, et al. RNA Methyltransferase FTSJ3 Regulates the Type I Interferon Pathway to Promote Hepatocellular Carcinoma Immune Evasion. *Cancer Res.* 2024;84(3):405-18.
35. Kato H, et al. Differential roles of MDA5 and RIG-I helicases in the recognition of RNA viruses. *Nature.* 2006;441(7089):101-5.
36. Watanabe A, et al. Association of aberrant ASNS imprinting with asparaginase sensitivity and chromosomal abnormality in childhood BCP-ALL. *Blood.* 2020;136(20):2319-33.
37. Uggenti C, et al. Self-Awareness: Nucleic Acid-Driven Inflammation and the Type I Interferonopathies. *Annu Rev Immunol.* 2019;37:247-67.
38. Hur S. Double-Stranded RNA Sensors and Modulators in Innate Immunity. *Annu Rev Immunol.* 2019;37:349-75.
39. Takeuchi O, and Akira S. Pattern recognition receptors and inflammation. *Cell.* 2010;140(6):805-20.
40. Goubau D, et al. Cytosolic sensing of viruses. *Immunity.* 2013;38(5):855-69.
41. Chen W, et al. Induction of Siglec-G by RNA viruses inhibits the innate immune response by promoting RIG-I degradation. *Cell.* 2013;152(3):467-78.
42. McGrail DJ, et al. High tumor mutation burden fails to predict immune checkpoint blockade response across all cancer types. *Ann Oncol.* 2021;32(5):661-72.
43. Nadal R, et al. Progress in systemic therapy for advanced-stage urothelial carcinoma. *Nat Rev Clin Oncol.* 2024;21(1):8-27.
44. Yuan H, et al. Lysine catabolism reprograms tumour immunity through histone crotonylation. *Nature.* 2023;617(7962):818-26.
45. Fang L, et al. Methionine restriction promotes cGAS activation and chromatin untethering through demethylation to enhance antitumor immunity. *Cancer Cell.* 2023;41(6):1118-33.e12.
46. Oh DY, et al. Intratumoral CD4(+) T Cells Mediate Anti-tumor Cytotoxicity in Human Bladder Cancer. *Cell.* 2020;181(7):1612-25.e13.
47. Wong JKM, et al. TGF-β signalling limits effector function capacity of NK cell anti-tumour immunity in human bladder cancer. *EBioMedicine.* 2024;104:105176.
48. Du G, et al. Retinoic acid-inducible gene-I like receptor pathway in cancer: modification and treatment. *Front Immunol.* 2023;14:1227041.
49. Xu XX, et al. RIG-I: a multifunctional protein beyond a pattern recognition receptor. *Protein Cell.* 2018;9(3):246-53.
50. Zhou P, et al. MLL5 suppresses antiviral innate immune response by facilitating STUB1-mediated RIG-I degradation. *Nat Commun.* 2018;9(1):1243.
51. Arimoto K, et al. Negative regulation of the RIG-I signaling by the ubiquitin ligase RNF125. *Proc Natl Acad Sci U S A.* 2007;104(18):7500-5.
52. Wang W, et al. RNF122 suppresses antiviral type I interferon production by targeting RIG-I CARDs to mediate RIG-I degradation. *Proc Natl Acad Sci U S A.* 2016;113(34):9581-6.

53. Wu S, et al. Targeting STING elicits GSDMD-dependent pyroptosis and boosts anti-tumor immunity in renal cell carcinoma. *Oncogene.* 2024;43(20):1534-48.
54. Wan J, et al. Astragaloside IV derivative HHQ16 ameliorates infarction-induced hypertrophy and heart failure through degradation of lncRNA4012/9456. *Signal Transduct Target Ther.* 2023;8(1):414.
55. Wang M, et al. Acquired semi-squamatization during chemotherapy suggests differentiation as a therapeutic strategy for bladder cancer. *Cancer Cell.* 2022;40(9):1044-59.e8.

Figures and Figure Legends

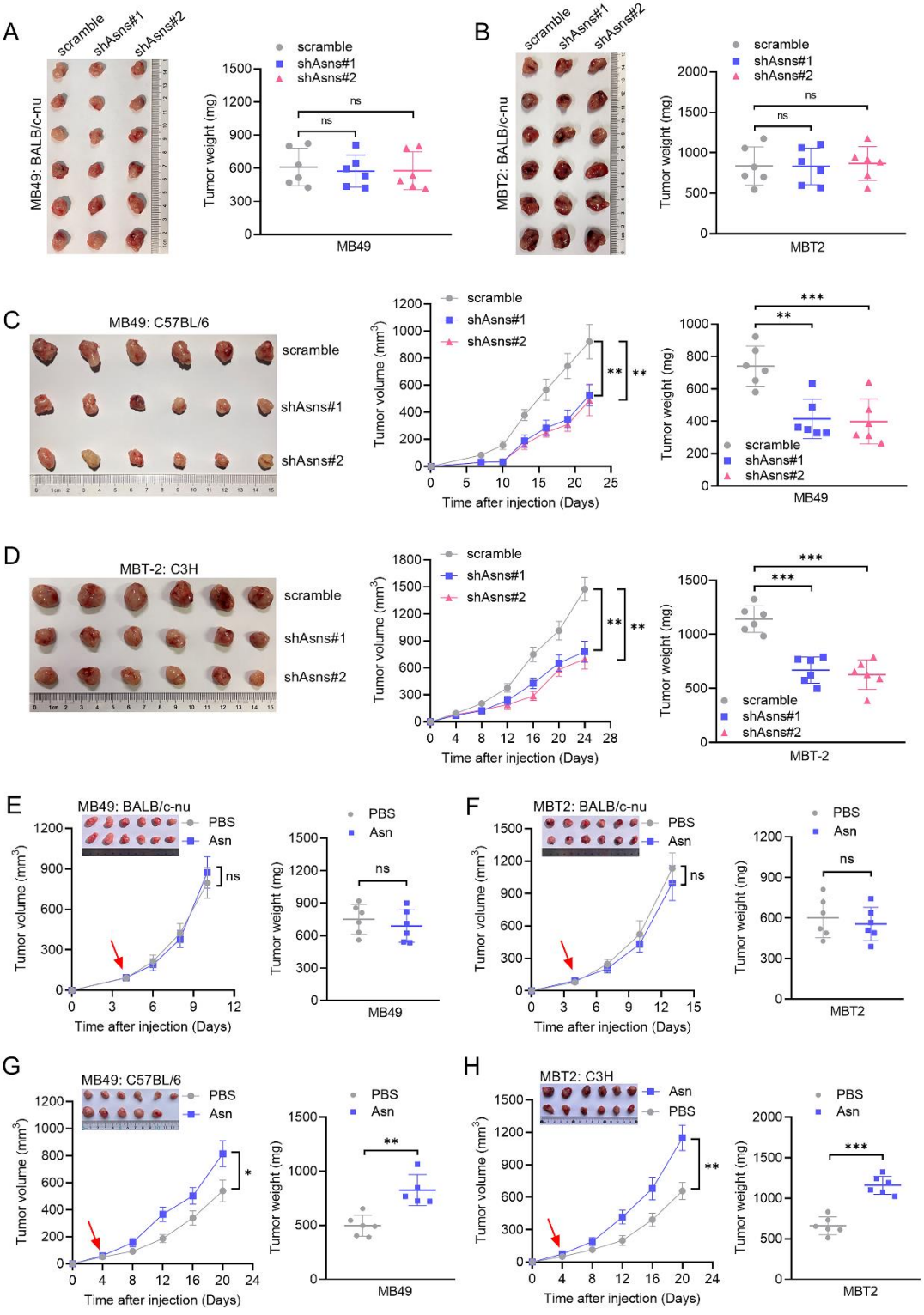

Figure 1. Asparagine restriction attenuates tumor growth in syngeneic mice.

(**A**) Tumor image and tumor weight of immunodeficient nude mice (n = 6) injected

subcutaneously with scramble or shAsns MB49 cells.

(**B**) Tumor image and tumor weight of immunodeficient nude mice (n = 6) injected subcutaneously with scramble or shAsns MBT2 cells.

(**C**) Tumor growth curves and tumor weight of immunocompetent C57BL/6 mice (n = 6) injected subcutaneously with scramble or shAsns MB49 cells.

(**D**) Tumor growth curves and tumor weight of immunocompetent C3H mice (n = 6) injected subcutaneously with scramble or shAsns MBT2 cells.

(**E**) Tumor growth curves and tumor weight of immunodeficient nude mice (n = 6) injected subcutaneously with MB49 cells administrated with PBS or Asn.

(**F**) Tumor growth curves and tumor weight of immunodeficient nude mice (n = 6) injected subcutaneously with MBT2 cells administrated with PBS or Asn.

(**G**) Tumor growth curves and tumor weight of immunocompetent C57BL/6 mice (n = 6) injected subcutaneously MB49 cells administrated with PBS or Asn.

(**H**) Tumor growth curves and tumor weight of immunocompetent C3H mice (n = 6) injected subcutaneously MBT2 cells administrated with PBS or Asn.

Data were mean ± SD. Statistical significance was calculated by two tailed unpaired Student's t-tests for E, F, G and H. One-way ANOVA for A, B, C and D. ns, not significant. **p<0.01, ***p<0.001.

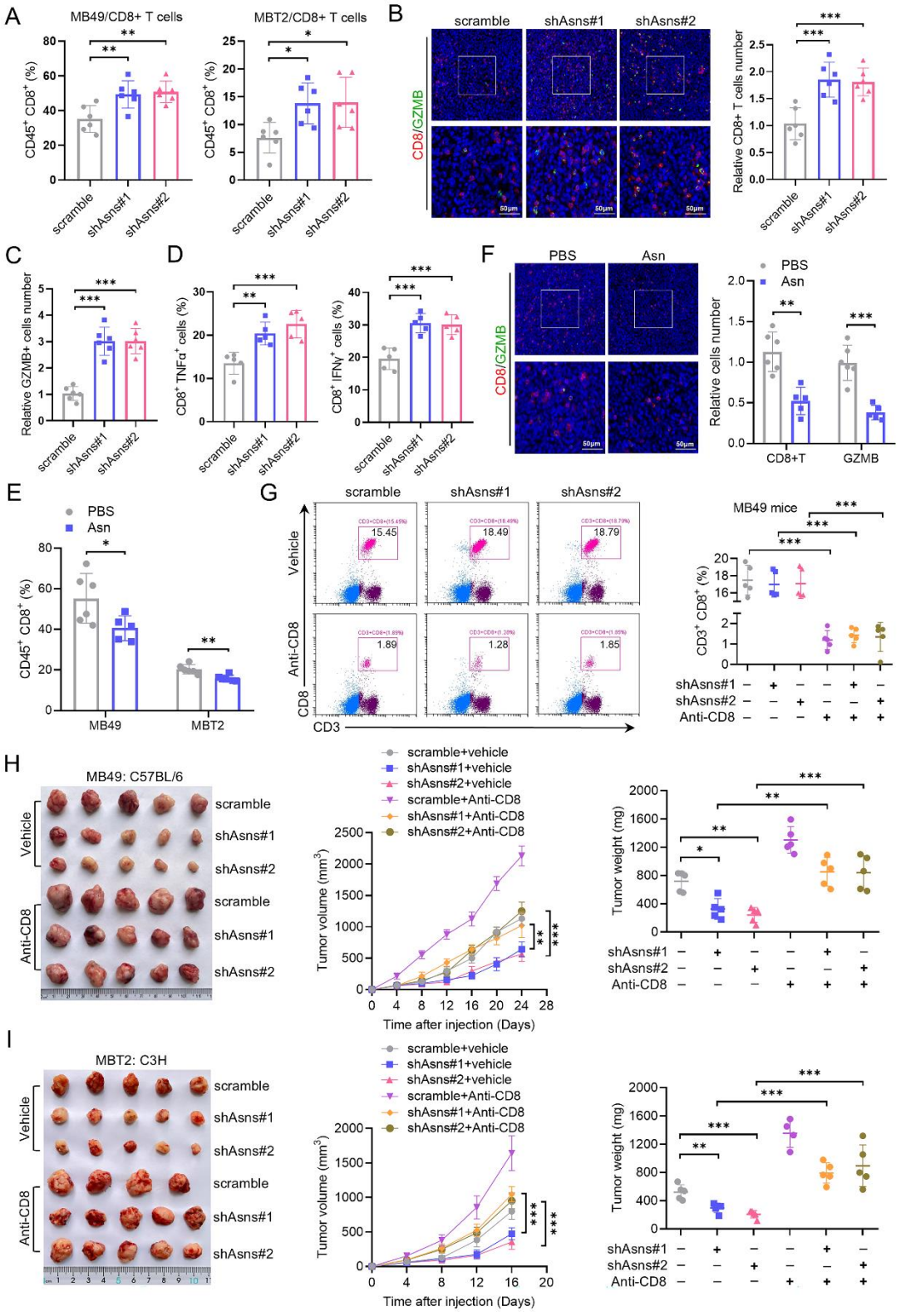

874

875 **Figure 2. Knockdown of ASNS potentiates antitumor function of CD8+ T cells.**

876 (**A**) Tumor infiltrating CD8+ T cells from transplanted shAsns-MB49 tumors (n = 6) in

877 C57BL/6 mice and shAsns-MBT2 tumors (n = 6) in C3H mice were analyzed by flow

cytometry.

(**B-C**) Representative images and quantification of immunofluorescence for CD8 (**B**) and GZMB (**C**) in scramble and shAsns-MB49 tumors (n = 6). Scale bars, 50 μm.

(**D**) Flow staining and frequency of CD8+TNFα+ and CD8+IFNγ+ cells in shAsns-MB49 and control tumors (n = 5).

(**E**) Tumor infiltrating CD8+ T cells were analyzed by flow cytometry from transplanted MB49 and MBT2 tumors (n = 6) in syngeneic mice administrated with PBS or Asn.

(**F**) Representative images and quantification of immunofluorescence for CD8 and GZMB in MB49 tumors administrated with PBS or Asn (n = 6). Scale bars, 50 μm.

(**G**) C57BL/6 mice were subcutaneously inoculated with MB49 tumor cells and treated with anti-CD8 antibody. Flow cytometry analysis of CD8+ T cells content in peripheral blood of mice (n = 5) at the end of experiment.

(**H**) Tumor growth curves and tumor weight from scramble and shAsns-MB49 tumor cells in C57BL/6 mice (n = 5) followed by intraperitoneal injection with anti-CD8 antibody.

(**I**) Tumor growth curves and tumor weight from scramble and shAsns-MBT2 tumor cells in C3H mice (n = 5) followed by intraperitoneal injection with anti-CD8 antibody.

Data were mean ± SD. Statistical significance was calculated by two tailed unpaired Student's t-tests for E and F. One-way ANOVA for A, B, C and D. Two-way ANOVA for G, H and I. *$p<0.05$, **$p<0.01$, ***$p<0.001$.

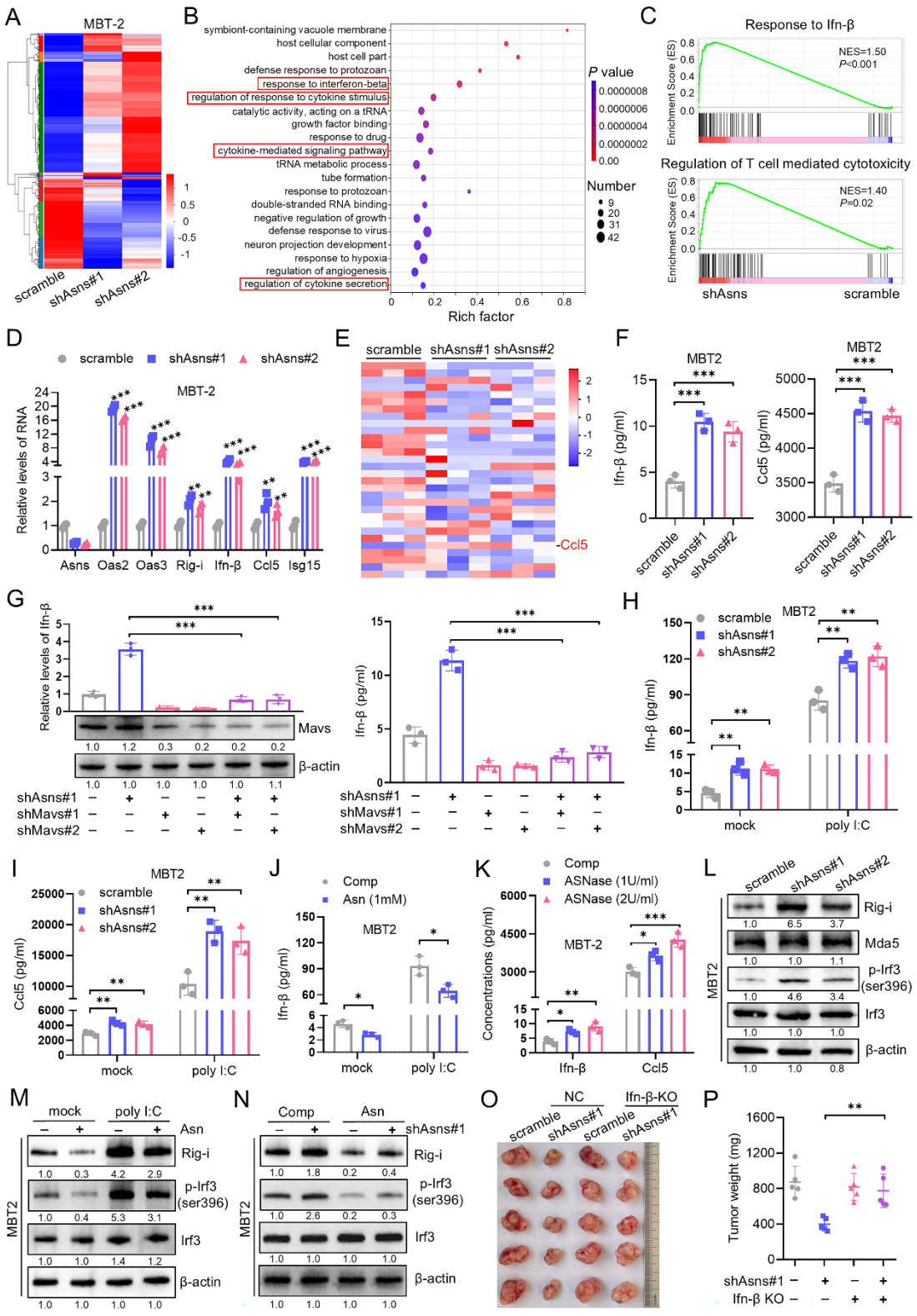

899

900 **Figure 3. Silencing of ASNS activates RIG-I-induced type I IFN signaling.**

901 (**A**) Heat map depicted the differentially expressed mRNA in the indicated MBT2 cells.

902 (**B**) Enrichment analysis for representative GO pathways in shAsns-mediated target

genes.

(**C**) GSEA plots of individual pathways enriched in shAsns-deficient MBT2 cells.

(**D**) qRT-PCR showed the relative expression levels of ISGs genes in the indicated MBT2 cells.

(**E**) Heatmap of multiple cytokines and chemokines detected by Luminex protein biochip testing system between Asns knockdown and the control groups in MBT2 cells culture supernatants.

(**F**) ELISA experiment revealed the expression levels of Ifn-β and Ccl5 in culture supernatants of the indicated MBT2 cells.

(**G**) qRT-PCR (left) and ELISA (right) assays showed the expression levels of Ifn-β in the indicated MBT2 cells. Western blot analysis of cell lysates from the indicated MBT2 cells.

(**H-I**) Scramble or shAsns MBT2 cells were transfected with poly (I:C) (2μg/ml) for 8 h and the protein levels of Ifn-β (**H**) and Ccl5 (**I**) were determined by ELISA.

(**J**) ELISA assay showed the expression levels of Ifn-β protein in the indicated MBT2 cells.

(**K**) ELISA assay showed the expression levels of Ifn-β and Ccl5 in MBT2 cells treated with ASNase for 48 h.

(**L**) Western blot analysis of cell lysates from the MBT2 cells stably transfected with scramble and shAsns.

(**M**) Western blot analysis of cell lysates from the indicated MBT2 cells.

(**N**) Western blot analysis of cell lysates from the indicated MBT2 cells.

(**O-P**) Tumor image and tumor weight of immunocompetent C57BL/6 mice (n = 5) injected subcutaneously with indicated MB49 cells.

Data were mean ± SD. Statistical significance was calculated by two tailed unpaired Student's t-tests for J. One-way ANOVA for D, F, H, I and K. Two-way ANOVA for G and P. *$p<0.05$, **$p<0.01$, ***$p<0.001$.

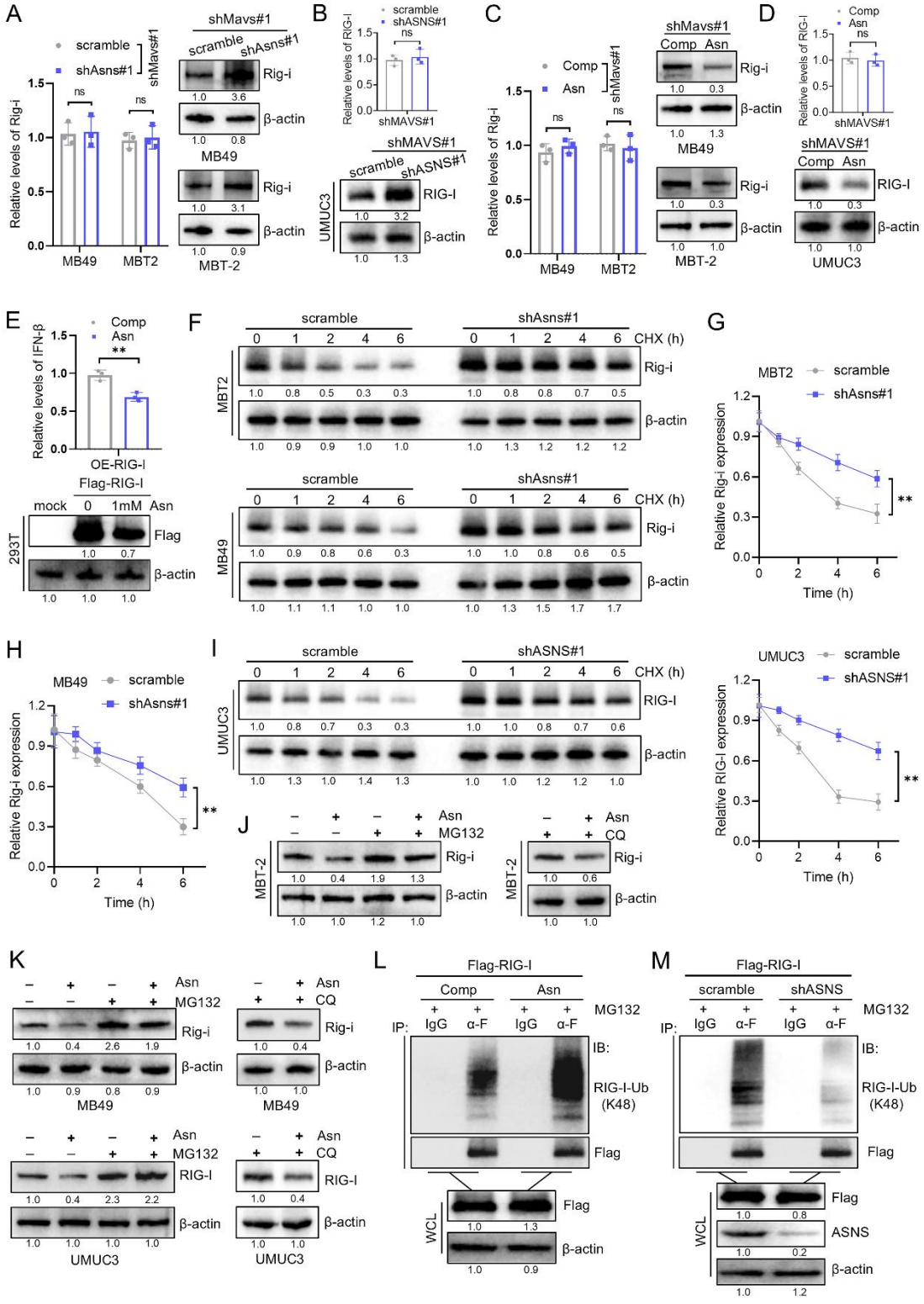

930

931 **Figure 4. Asparagine facilitates the ubiquitination degradation of RIG-I.**

932 (**A**) qRT-PCR and western blot showed the expression levels of Rig-i mRNA and

933 protein in the indicated Murine bladder cancer cells.

(**B**) qRT-PCR and western blot showed the expression levels of RIG-I mRNA and protein in the indicated UMUC3 cells.

(**C**) qRT-PCR and western blot showed the expression levels of Rig-i mRNA and protein in the indicated Murine bladder cancer cells.

(**D**) qRT-PCR and western blot showed the expression levels of RIG-I mRNA and protein in the indicated UMUC3 cells.

(**E**) qRT-PCR showed the expression levels of IFN-β in RIG-I-overexpressed HEK293T cells cultured in complete medium (Comp) and medium added Asn (1mM) for 48 h. Western blot showed the levels of RIG-I protein in the indicated groups.

(**F-H**) Western blot revealed the degradation kinetics of Rig-i protein in the indicated Murine bladder cancer cells. The degradation rate of Rig-i protein was quantified by band intensity.

(**I**) Western blot revealed the degradation kinetics of RIG-I protein in in the indicated UMUC3 cells. The degradation rate of RIG-I protein was quantified by band intensity.

(**J**) Western blot analysis showed the Rig-i expression in the indicated MBT2 cells.

(**K**) Western blot analysis showed the RIG-I expression in the indicated MB49 or UMUC3 cells.

(**L**) HEK293T cells were transfected with Flag-RIG-I and cultured in complete medium (Comp) or medium added Asn (1mM) for 48 h, followed by co-immunoprecipitation and immunoblotting analysis with the indicated antibodies.

(**M**) HEK293T cells were transfected with Flag-RIG-I and with scramble or shASNS#1 for 48 h, followed by co-immunoprecipitation and immunoblotting analysis with the indicated antibodies.

Data were mean ± SD. Statistical significance was calculated by two tailed unpaired Student's t-tests for A, B, C, D, E, G, H and I. ns, not significant. **$p<0.01$.

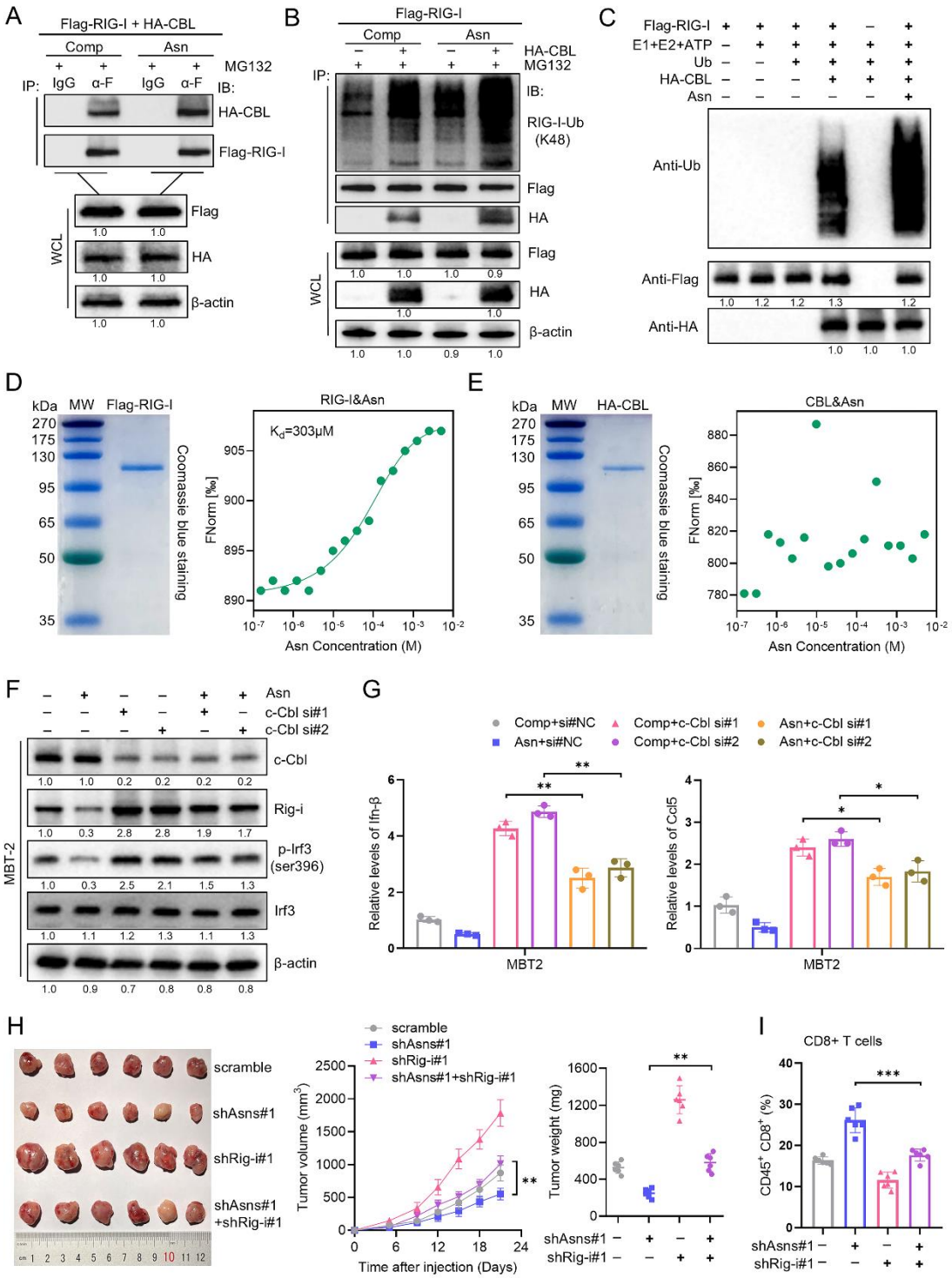

959

960 **Figure 5. Asparagine promotes the CBL-mediated proteasomal degradation of**

961 **RIG-I.**

962 (**A**) HEK293T cells were transfected with Flag-RIG-I and HA-CBL and cultured in

963 complete medium (Comp) and medium added Asn (1mM) for 48 h, followed by co-
964 immunoprecipitation and immunoblotting analysis with the indicated antibodies.
965 (**B**) Flag-RIG-I-overexpressed HEK293T cells were cultured in complete medium
966 (Comp) or medium added Asn (1mM), and those co-transfected with a control and HA-
967 CBL overexpression plasmid for 48 h, followed by co-immunoprecipitation and
968 immunoblotting analysis with the indicated antibodies.
969 (**C**) Purified Flag-RIG-I proteins were incubated with the indicated proteins in the
970 presence or absence of 1 mM Asn for 2 h. Mixtures were analyzed by western blot.
971 (**D**) MST measurement of the interaction between Asn and purified RIG-I. Kd value
972 was automatically by the curve fitting.
973 (**E**) MST measurement of the interaction between Asn and purified CBL.
974 (**F**) Western blot of the indicated proteins in MBT2 cells cultured in complete medium
975 (Comp) or medium added Asn (1mM), and those co-transfected with si-NC, si-Cbl#1
976 or si-Cbl#2.
977 (**G**) qRT-PCR revealed the expression levels of Ifn-β and Ccl5 in MBT2 cells cultured
978 in complete medium (Comp) or medium added Asn (1mM), and those co-transfected
979 with si-NC, si-Cbl#1 or si-Cbl#2.
980 (**H**) Tumor growth curves and tumor weight of immunocompetent C3H mice (n = 6)
981 injected subcutaneously with indicated MBT2 cells.
982 (**I**) Tumor infiltrating CD8+ T cells from transplanted MBT2 tumors (n = 6) in C3H
983 mice were analyzed by flow cytometry.
984 Data were mean ± SD. Statistical significance was calculated by two-way ANOVA for
985 G, H and I. *$p<0.05$, **$p<0.01$, ***$p<0.001$.

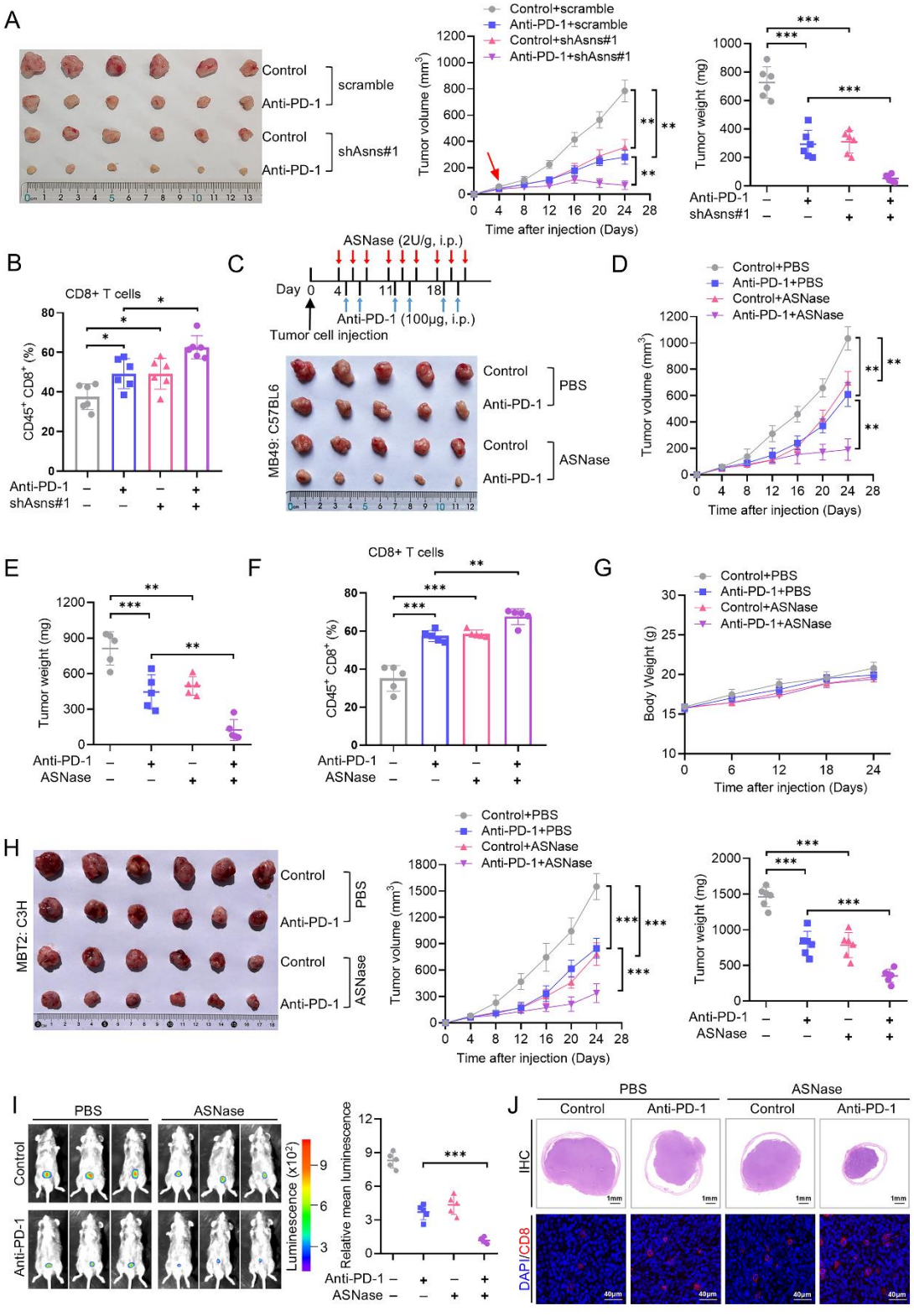

986

987 **Figure 6. Asparagine restriction overcomes tumor resistance to PD-1 blockade in**

988 **mouse model.**

989 (**A**) Tumor growth and tumor weight in immunocompetent C57BL/6 mice injected

subcutaneously with MB49 cells stably transfected with scramble and shAsns#1, and treated with anti-PD-1 or isotype control (n = 6).

(**B**) Flow cytometry showed the tumor infiltrating CD8+ T cells in MB49 tumors of indicated groups.

(**C-E**) Schematic of ASNase therapy. Tumor growth and tumor weight in immunocompetent C57BL/6 mice injected subcutaneously with MB49 cells administrated with ASNase, and treated with anti-PD-1 or isotype control (n = 5).

(**F**) Tumor infiltrating CD8+ T cells in MB49 tumors of indicated groups were analyzed by flow cytometry.

(**G**) The body weights among different groups during experimental procedure.

(**H**) Tumor image and tumor weight in immunocompetent C3H mice injected subcutaneously with MBT2 cells administrated with ASNase, and treated with anti-PD-1 or isotype control (n = 6).

(**I**) Representative luminescence images and histogram analysis of bioluminescence intensity in C57BL/6 mice injected orthotopically with luc-labeling MB49 cells with the treatment of ASNase and anti-PD-1 antibody.

(**J**) Representative hematoxylin and eosin (H&E) staining and immunofluorescence for CD8 of tumors in the indicated groups. H&E staining, scale bars, 1 mm. Immunofluorescence staining, scale bars, 40 μm.

Data were mean ± SD. Statistical significance was calculated by two-way ANOVA for A, B, D, E, F, H and I. ns, not significant. *p<0.05, **p<0.01, ***p<0.001.

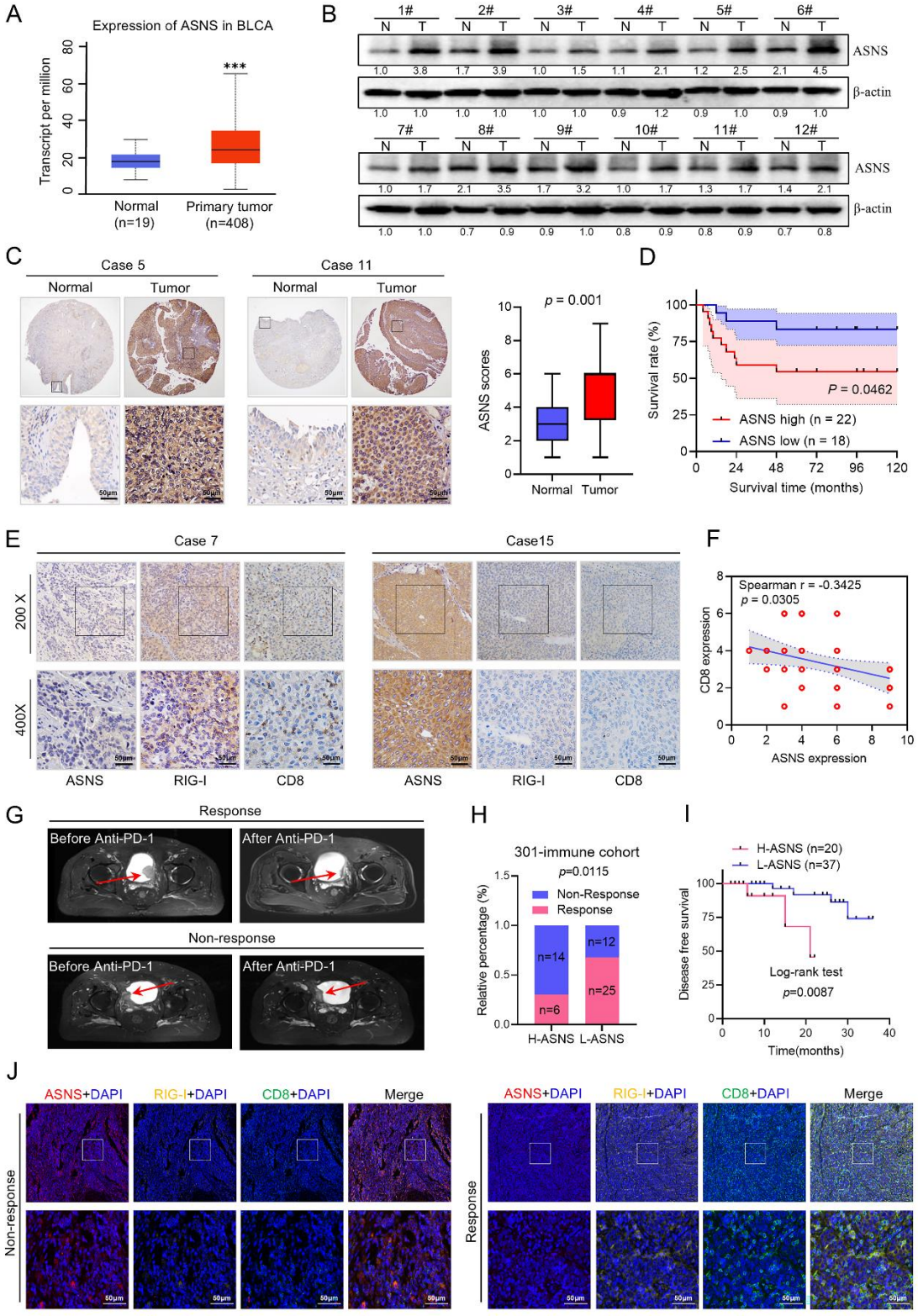

Figure 7. Upregulated ASNS leads bladder cancer resistance to ICIs.

(**A**) mRNA levels of ASNS in bladder cancer samples from TCGA cohort.

(**B**) Western blot showed the expression levels of ASNS in our paired samples of

bladder cancer.

(**C**) Representative IHC staining and quantification revealed ASNS expression in paired samples of bladder cancer from our cohort (n = 40). Scale bar, 50 μm.

(**D**) Kaplan-Meier analysis of the overall survival of 40 patients with high or low expression of ASNS.

(**E**) Representative IHC staining of ASNS, RIG-I and CD8 in bladder cancer samples from our cohort.

(**F**) Correlation analysis of ASNS expression and CD8 expression in bladder cancer clinical samples (n = 40).

(**G**) Representative MRI image for patient with response and non-response after ICIs treatment in our hospital (301-immune cohort, n = 57).

(**H**) The relationship between ASNS expression level and immunotherapy efficacy in 301- immune cohort.

(**I**) Disease-free survival of patients with different ASNS IHC scores in our immune cohort.

(**J**) Representative multi-color IF images for ASNS (red), RIG-I (yellow), CD8 (green) and DAPI (blue) in response and non-response group patients. Scale bars, 50 μm.

Data were mean ± SD. Statistical significance was calculated by two tailed unpaired Student's t-tests for A. Paired Student's t-tests for C. Chi-square test for H. Survival analysis of D and I was performed by the log-rank test. ***$p<0.001$.